

# Patient-specific computational flow modelling for assessing hemodynamic changes following fenestrated endovascular aneurysm repair

Kenneth Tran, MD,<sup>a,b</sup> Weiguang Yang, PhD,<sup>c</sup> Alison Marsden, PhD,<sup>c,d</sup> and Jason T. Lee, MD,<sup>a,b</sup> Stanford, Calif

## ABSTRACT

**Objective:** This study aimed to develop an accessible patient-specific computational flow modelling pipeline for evaluating the hemodynamic performance of fenestrated endovascular aneurysm repair (fEVAR), with the hypothesis that computational flow modelling can detect aortic branch hemodynamic changes associated with fEVAR graft implantation.

**Methods:** Patients who underwent fEVAR for juxtarenal aortic aneurysms with the Cook ZFEN were retrospectively selected. Using open-source SimVascular software, preoperative and postoperative visceral aortic anatomy was manually segmented from computed tomography angiograms. Three-dimensional geometric models were then discretized into tetrahedral finite element meshes. Patient-specific pulsatile in-flow conditions were derived from known supraceliac aortic flow waveforms and adjusted for patient body surface area, average resting heart rate, and blood pressure. Outlet boundary conditions consisted of three-element Windkessel models approximated from physiologic flow splits. Rigid wall flow simulations were then performed on preoperative and postoperative models with the same inflow and outflow conditions. We used SimVascular's incompressible Navier-Stokes solver to perform blood flow simulations on a cluster using 72 cores.

**Results:** Preoperative and postoperative flow simulations were performed for 10 patients undergoing fEVAR with a total of 30 target vessels (20 renal stents, 10 mesenteric scallops). Postoperative models required a higher mean number of mesh elements to reach mesh convergence ( $3.2 \pm 1.8 \times 10^6$  vs  $2.6 \pm 1.1 \times 10^6$ ;  $P = .005$ ) with a longer mean computational time ( $10.3 \pm 6.3$  hours vs  $7.8 \pm 3.5$  hours;  $P = .04$ ) compared with preoperative models. fEVAR was associated with small but statistically significant increases in mean peak proximal aortic arterial pressure ( $140.3 \pm 11.0$  mm Hg vs  $136.9 \pm 8.7$  mm Hg;  $P = .02$ ) and peak renal artery pressure ( $131.6 \pm 14.8$  mm Hg vs  $128.9 \pm 11.8$  mm Hg;  $P = .04$ ) compared with preoperative simulations. No differences were observed in peak pressure in the celiac, superior mesenteric, or distal aortic arteries ( $P = .17-.96$ ). When measuring blood flow, the only observed difference was an increase in peak renal flow rate after fEVAR ( $17.5 \pm 3.8$  mL/s vs  $16.9 \pm 3.5$  mL/s;  $P = .04$ ). fEVAR was not associated with changes in the mean pressure or the mean flow rate in the celiac, superior mesenteric, or renal arteries ( $P = .06-.98$ ). Stenting of the renal arteries did not induce significant changes time-averaged wall shear stress in the proximal renal artery ( $23.4 \pm 8.1$  dynes/cm<sup>2</sup> vs  $23.2 \pm 8.4$  dynes/cm<sup>2</sup>;  $P = .98$ ) or distal renal artery ( $32.7 \pm 13.9$  dynes/cm<sup>2</sup> vs  $29.6 \pm 11.8$  dynes/cm<sup>2</sup>;  $P = .23$ ). In addition, computational visualization of cross-sectional velocity profiles revealed low flow disturbances associated with protrusion of renal graft fabric into the aortic lumen.

**Conclusions:** In a pilot study involving a selective cohort of patients who underwent uncomplicated fEVAR, patient-specific flow modelling was a feasible method for assessing the hemodynamic performance of various two-vessel fenestrated device configurations and revealed subtle differences in computationally derived peak branch pressure and blood flow rates. Structural changes in aortic flow geometry after fEVAR do not seem to affect computationally estimated renovisceral branch perfusion or wall shear stress adversely. Additional studies with invasive angiography or phase contrast magnetic resonance imaging are required to clinically validate these findings. (*JVS—Vascular Science* 2021;2:53-69.)

**Clinical Relevance:** Using a computational flow modelling for assessing the hemodynamic performance of fenestrated endovascular aneurysm repair (fEVAR), this real-world, patient-specific study included 10 participants and found that structural changes in aortic flow geometry after fEVAR did not seem to adversely impact estimated renal or visceral branch perfusion metrics (eg, peak and mean arterial pressure and flow rates) or wall shear stress. These findings overall support the ongoing clinical use of commercially available fEVAR devices for repair of juxtarenal aortic aneurysms, and provides a computational framework for future evaluation of fEVAR configurations in a preoperative or postoperative settings.

**Keywords:** Fenestrated endovascular aneurysm repair; Computational fluid dynamics; fEVAR; CFD; thrombosis; Patient-specific

From the Division of Vascular Surgery,<sup>a</sup> Cardiovascular Institute,<sup>b</sup> Department of Pediatrics (Cardiology),<sup>c</sup> and the Department of Bioengineering,<sup>d</sup> Stanford University.

This work was funded by NIH T32 grant 2T32HL09804911 (K.T.).

Author conflict of interest: none.

Correspondence: Kenneth Tran, MD, Division of Vascular Surgery, Stanford University, 300 Pasteur Dr, Alway Building M121, Stanford CA 94305 (e-mail: [kenneth.tran@stanford.edu](mailto:kenneth.tran@stanford.edu)).

The editors and reviewers of this article have no relevant financial relationships to disclose per the JVS-Vascular Science policy that requires reviewers to decline review of any manuscript for which they may have a conflict of interest.

2666-3503

Copyright © 2021 by the Society for Vascular Surgery. Published by Elsevier Inc.

This is an open access article under the CC BY-NC-ND license (<http://creativecommons.org/licenses/by-nc-nd/4.0/>).

<https://doi.org/10.1016/j.jvssci.2020.11.032>

Over the past decade, fenestrated endovascular aneurysm repair (fEVAR) has grown to be a widely practiced technique for the repair of juxtarenal aortic aneurysms, with multiple centers using fEVAR as the new standard of care for high-physiologic risk patients with a hostile infrarenal neck.<sup>1-3</sup> In the United States, the ZFEN device (ZFEN, Cook Medical, Bloomington, Ind) remains the only commercially approved device available for fEVAR, with multiple studies supporting durable short-term and midterm outcomes.<sup>4-7</sup> Nonetheless, concerns remain regarding the risk of renal branch graft complications, including stenosis and occlusion, as well as long-term renal function decline, which sometimes occurs without identifiable underlying anatomic or structural causes.<sup>8,9</sup> In addition, renal stents placed within fenestrations require graft fabric protrusion into the aortic lumen to achieve aneurysm exclusion. This may affect local hemodynamic parameters that are difficult to study with current clinical imaging techniques.

Computational fluid dynamics (CFD) have been commonly used in a variety of engineering branches, ranging from aerodynamics to petroleum engineering. It has recently found applications in cardiovascular disease for modelling postsurgical changes in flow parameters such as arterial pressure, blood flow rate, and wall shear stress.<sup>10-12</sup> Measurement of CFD model-derived hemodynamic parameters have further been validated in *in vitro* and *in vivo* models, strengthening the clinical applicability of these novel methods in various vascular pathologies.<sup>13-19</sup> Owing to the complexity of model generation, flow simulation, and analytics, CFD techniques have only been applied in limited fashion for assessing outcomes after complex EVAR, with existing studies limited to extremely small sample sizes and often using idealized, non-patient-specific models.<sup>20-25</sup>

In recent years, proponents of CFD modelling have created significant advancements by developing validated, open source software packages designed specifically to simulate human arterial blood flow.<sup>26,27</sup> These packages allow researchers to perform all steps of CFD model creation and simulation within an efficient and easy-to-understand graphic user interface, thus allowing CFD techniques to be used by a wider audience. The goal of this study was thus to develop an accessible, patient-specific CFD modelling pipeline for evaluating the hemodynamic performance of fEVAR using routinely obtained, noninvasive preoperative and postoperative imaging in a cohort of patients undergoing elective fEVAR. We hypothesized that computational flow modelling can detect aortic branch hemodynamic changes associated with fEVAR graft implantation.

## METHODS

**Patient cohort.** A retrospective chart and radiologic review was performed on a prospectively maintained database involving all patients undergoing elective fEVAR at

## ARTICLE HIGHLIGHTS

- **Type of Research:** Computational flow simulation of data from a single institution
- **Key Findings:** Fenestrated endovascular aneurysm repair (fEVAR) was associated with small but statistically significant increases in the peak proximal aortic pressure ( $140.3 \pm 11.0$  vs  $136.9 \pm 8.7$  mm Hg;  $P = .02$ ) and peak renal artery pressure ( $131.6 \pm 14.8$  vs  $128.9 \pm 11.8$  mm Hg;  $P = .04$ ), with a corresponding increase in peak renal flow rate after fEVAR ( $17.5 \pm 3.8$  vs  $16.9 \pm 3.5$  mL/s;  $P = .04$ ). Stenting of the renal arteries did not induce significant changes in the time-averaged wall shear stress in the proximal renal artery ( $23.4 \pm 8.1$  vs  $23.2 \pm 8.4$  dynes/cm<sup>2</sup>;  $P = .98$ ) or distal renal artery ( $32.7 \pm 13.9$  vs  $29.6 \pm 11.8$  dynes/cm<sup>2</sup>;  $P = .23$ ).
- **Take Home Message:** Structural changes in aortic flow geometry after fEVAR do not seem to affect computationally estimated renal or visceral branch perfusion adversely. Patient-specific flow modelling is a feasible method for assessing the hemodynamic performance of fEVAR device configurations.

a single institution between 2012 and 2019. For the purposes of this pilot study, we only included patients who were treated within the device instructions for use, without postoperative graft-related complications (eg, proximal endoleak, branch stenosis) and also those who had adequate computed tomography angiography (CTA) imaging available for review. In addition, a range of main body graft diameters (24-36 mm) was purposefully selected. Of 85 eligible patients, we selected 10 representative patients who had ZFEN grafts implanted with a range of main body graft diameters (24-36 mm). Neither patient sex nor race were used as specific selection criteria. All patients received a custom ZFEN graft with two proximal seal stents, two 6-mm renal fenestrations, and either a scallop or large fenestration for the superior mesenteric artery. Either iCAST (Atrium USA, Hudson, NH) or Viabahn VBX (W. L. Gore & Associates, Flagstaff, Ariz) stents were used as renal branch grafts. This study was approved by our institutional review board. Owing to the retrospective nature of the study, signed informed consent was not obtained.

**Clinical data.** CTA is routinely performed preoperatively or postoperatively for patients undergoing fEVAR. For this study, we used high-resolution CTA imaging with 0.80- to 1.25-mm slices to obtain preoperative and postoperative aneurysm and stent graft morphology. The first postoperative CT scan was used for fEVAR modelling, which was obtained within 30 days of the index procedure. Commonly available hemodynamic parameters, including average outpatient systolic and diastolic

blood pressure (mm Hg), heart rate (beats per second), as well as height (m) and weight (kg), were also collected to derive a patient-specific allometrically scaled supraceliac inflow waveform.<sup>28</sup>

**Image segmentation, three-dimensional (3D) modeling, and mesh generation.** Using the built-in image segmentation toolkit, preoperative and postoperative 3D models were created by lofting manually segmented two-dimensional splines of vessels lumens based on center-line CTA images (Fig 1, A and B). For the purposes of examining the visceral branch flow, the celiac, superior mesenteric, and renal arteries were all segmented up to the first major branch point. The aortic anatomy was modelled from the midthoracic aorta until the aortic bifurcation or flow divider in postoperative models. Modelling of the proximal aorta well above the region of interest is important to allow for the development of uniform flow during simulation. To decrease computational cost, the iliac and lumbar arteries were excluded from segmentation. Two-dimensional splines were then lofted into 3D models using the built-in SimVascular operation.

The construction of postoperative models required an additional modelling step to create the unique geometry associated with renal branch graft protrusion into the aortic lumen. Aortic and visceral/renal branch models created in SimVascular were exported to Rhino3D (McNeel Associates, Seattle, Wash). Using Boolean scaling, addition and subtracting operations, flared renal graft segments were created with approximately 0.5-mm thickness (Fig 1, C). These new models were then imported back into the SimVascular for additional processing.

Constructed 3D models were then discretized into tetrahedral elements using an open source mesh generator, TetGen, which was integrated into Simvascular.<sup>29</sup> Mesh convergence studies were performed which demonstrated that a minimum mesh size of approximately 0.65 mm led to less than 1% variance in recorded outlet pressure and flow rates and less than 5% variance in time-averaged wall-shear stress. Therefore, a 0.5-mm minimum mesh size was used for all areas of interest (paravisceral aorta and branches) using regional mesh refinement (Fig 1, D). Areas outside the region of interest was meshed to 1 mm to decrease the computational time.

**Boundary condition specification.** Phase contrast magnetic resonance imaging (PC-MRI) has been used to obtain patient-specific inflow waveforms. However, PC-MRI studies are expensive and not routinely performed for patients undergoing fEVAR. A supraceliac pulsatile inflow waveform obtained by PC-MRI from patients with infrarenal abdominal aortic aneurysms was allometrically scaled and prescribed at the proximal thoracic aortic inlet following Les et al.<sup>28</sup> At each vessel

outlet, a lumped parameter model (three-element Windkessel model), which consists of three parameters: a proximal resistor, capacitor, and distal resistor was used to represent the resistance and compliance of the downstream vascular bed.<sup>11</sup> Using the preoperative model, proximal resistor, capacitor, and distal resistor parameters were tuned to the patient's blood pressure and expected physiologic flow splits from the literature. Specifically, 25% of the inlet flow was assigned to the celiac artery, 31% to the superior mesenteric artery, 22% to each renal artery, and the remaining assigned to the distal aortic outlet.<sup>30</sup> For mesenteric and distal aortic outlets, the majority of the resistance was assumed to be caused by downstream vascular bed and thus 94.4% of resistance was assigned the distal resistor parameter. For the renal arteries, 72% of the total resistance was assigned to the distal resistor to account for low-resistance renal flow.<sup>23</sup>

**Flow simulation.** Blood viscosity was assumed to be Newtonian with a viscosity of 0.04 P with a density of 1.06 g/cm<sup>3</sup>. Walls were defined as rigid with a no-slip boundary condition. Flow simulations were performed by solving the incompressible Navier-Stokes equation using a stabilized finite element solver<sup>31-33</sup> on a cluster using 72 processors. The final models were run with a step size of 1/500th of a cardiac cycle (approximately 0.002 second), with the total simulation running a total of five cardiac cycles. The minimum residuals required was  $1 \times 10^{-4}$ . Results from the last cardiac cycle were saved with a sampling frequency of 50 per cardiac cycle.

**Parameter analysis and statistics.** Hemodynamic parameters including pressure waveforms, flow rates and time-averaged wall shear stress (tWSS) at the branches were calculated. These values were compared between preoperative and postoperative models using signed Wilcoxon rank-sum tests to assess for paired patient differences. For categorization, the increased peak pressure and flow were defined as an increase of at least 1 mm Hg and 0.5 mL/s, respectively, in the postoperative model. A decreased peak pressure and flow was defined as a decrease of at least 1 mm Hg and 0.5 mL/s, respectively. Unchanged peak pressure and flow was defined as between -1 and 1 mm Hg change, and -0.5 mL/s and +0.5 mL/s change, respectively. A *P* value of less than .05 was considered statistically significant for all analyses. All calculations were performed in Stata SE16.0 (Stata-Corp LP, College Station, Tex). Paraview Visualization ToolKit (Los Alamos National Laboratory, Santa Fe, NM) was used for visualization of tWSS and local velocity fields.

## RESULTS

Patient-specific 3D modelling and flow simulations were performed on 10 patients undergoing fEVAR.

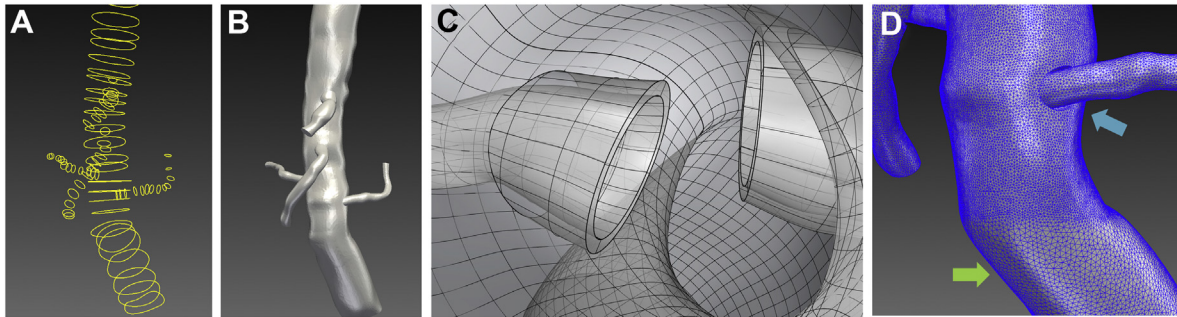


**Fig 1.** **A**, Manually created two-dimensional (2D) spline contours along the center lines of the aorta and visceral branches. **B**, A three-dimensional lofted model from a series of 2D contours. **C**, Manually created intra-aortic renal graft fabric of 0.5 mm thickness simulating the flared renal stent graft protruding into the aortic lumen. **D**, Regional mesh refinement demonstrating smaller mesh element size of 0.5 mm (blue arrow) and 1.0 mm (green arrow).

Anatomic and device-related variables for each patient are listed in Table I. Notably, a range of main body endograft diameters were included (24–36 mm) as well as neck angulation ( $0^{\circ}$ – $90^{\circ}$ ). Several of the patients ( $n = 5$  [50%]) had either unilateral ( $n = 4$ ) or bilateral ( $n = 1$ ) renal stenosis. The majority of patients underwent renal branch grafting with the iCAST stent ( $n = 9$  [90%]) with a scallop placed for the superior mesenteric artery. There were no instances of renal stent graft or distal artery stenosis or kinking, with no acute angulations found at the distal renal stent interface.

**Model complexity and computational time.** The 3D model generation required between 1 and 2 hours to manually segmented the geometry of interest. Owing to the increased geometric complexity associated with the flared renal graft fabric, postoperative models resulted in a larger number of mean mesh elements compared with preoperative models ( $3.2 \pm 1.8 \times 10^6$  vs  $2.6 \pm 1.1 \times 10^6$ ;  $P = .005$ ). This increased number of mesh elements also required longer mean computational times compared with preoperative models ( $10.3 \pm 6.3$  hours vs  $7.8 \pm 3.5$  hours using 72 processors;  $P = .04$ ).

**Aortic and arterial branch pressures.** Pressure waveforms were generated from each simulation on preoperative and postoperative models. The peak and mean arterial pressure at the aortic inlet (proximal aorta), aortic outlet (distal aorta/proximal to the flow divider), and arterial branch pressures were extracted and listed in Table II. On paired analysis between preoperative and postoperative models, fEVAR resulted in a statistically significant increase in peak proximal aortic pressure (140.3 mm Hg vs 136.9 mm Hg;  $P = .02$ ). A small but statistically significant increase in mean proximal aortic pressure was also observed (101.7 mm Hg vs 100.9 mm Hg;  $P = .04$ ). Renal branch grafting was also associated with an increased in peak renal artery pressure (131.6 mm Hg vs 128.9 mm Hg;  $P = .04$ ) but not mean renal pressure

(98.3 mm Hg vs 97.3 mm Hg;  $P = .30$ ). Of the 20 stented renal arteries, the most commonly observed change after fEVAR was an increase in peak renal pressure ( $n = 13$  [65%]), with an unchanged peak renal pressure ( $n = 3$  [15%]) or decreased peak renal pressure ( $n = 4$  [20%]) being less common (Fig 2). There were no observed trends or significant changes observed in the celiac or superior mesenteric arteries after fEVAR ( $P = .28$ – $.96$ ). Distal aortic pressure trended toward increased peak (141.7 mm Hg vs 138.8 mm Hg;  $P = .17$ ) and mean pressures (101.7 mm Hg vs 100.9 mm Hg;  $P = .06$ ) but did not reach significance.

**Aortic and arterial branch flow rates.** Peak and mean arterial flow rates are shown in Table II. The proximal aortic (inlet) flow rates are not shown owing to being a fixed inflow parameter between preoperative and postoperative models. There was an observed 3.5% mean increase in renal artery peak flow rate (17.5 mL/s vs 16.9 mL/s;  $P = .04$ ) after fEVAR, with no observed change in mean flow rate (7.8 mL/s vs 7.8 mL/s;  $P = .92$ ). Similar to observed changes in peak renal pressure, fEVAR was most commonly associated with increased peak renal flow in the majority of patients ( $n = 10$  [50%]), with unchanged ( $n = 6$  [30%]) and decreased peak renal flow ( $n = 4$  [20%]) being less common (Fig 2). There were no observed differences in the celiac or superior mesenteric arterial flow rates ( $P = .28$ – $.72$ ). In the distal aorta, fEVAR caused a trend toward increased peak (95.5 mL/s vs 92.0 mL/s;  $P = .16$ ) and mean (18.0 mL/s vs 17.9 mL/s;  $P = .06$ ) flow rates. A representative patient simulation demonstrating the changes in pressure and flow after fEVAR is shown in Fig 3.

**Correlation between renal hemodynamics and renal function.** In total, seven patients (70%) experienced computational estimated improved renal perfusion (Appendixes 1–7), two patients (20%) with no change in renal perfusion (Appendixes 8 and 9), and one (10%) with decreased renal perfusion after fEVAR (Appendix 10). All

**Table I.** Anatomic and device-related variables for each study patient

Patient	Aneurysm diameter, mm	Neck diameter, mm	Infrarenal angulation (°)	Main-body graft diameter, mm	Preoperative renal stenosis (% narrowing)	Left renal stent	Left renal stent-artery angulation (°)	Right renal stent	Right renal stent-artery angulation (°)	Superior mesenteric artery orifice
1	57	24	0	30	Left (80)	7 × 22 iCAST	50	7 × 22 iCAST	55	None
2	59	22	15	24	Right (60)	6 × 22 iCAST	30	6 × 22 iCAST	40	Scallop
3	63	28	25	34	None	6 × 22 iCAST	50	6 × 22 iCAST	10	Scallop
4	51	20	20	26	Left (60)	5 × 22 iCAST	5	5 × 22 iCAST	60	Scallop
5	58	24	27	30	Right (60)	7 × 22 iCAST	0	7 × 22 iCAST	40	Scallop
6	84	27	50	32	None	7 × 22 iCAST	20	7 × 22 iCAST	5	Scallop
7	55	24	20	28	None	7 × 22 iCAST	0	7 × 22 iCAST	0	Scallop
8	56	30	10	36	None	6 × 22 iCAST	35	6 × 22 iCAST	60	Scallop
9	57	18	90	24	Bilateral (70 right; 50 left)	6 × 22 iCAST	20	7 × 22 iCAST	0	Scallop
10	82	29	40	34	None	6 × 29 VB ×	5	6x29 VBX	40	Fenestration

five patients with evidence of preoperative renal stenosis had improvement in estimated renal perfusion (Appendixes 1-4, and 6). Four patients in this series had renal function decline (glomerular filtration rate decrease of >20% during follow-up), of which three patients (75%) had either unchanged or decreased estimated renal perfusion. The remaining six patients with either no change in renal function (or improved renal function) during follow-up all had increased estimated renal perfusion after fEVAR.

**Wall shear stress at aortic branches.** We calculated the tWSS in the unstented celiac and superior mesenteric arteries (Fig 4, A). For renal artery analysis, tWSS was calculated at two areas—in the stented portion of the artery and the unstented distal renal artery up to the first branch point (Fig 4, B). Preoperative mean tWSS were all within the physiologic range of 10 to 70 dynes/cm<sup>2</sup> for all models. fEVAR did not significantly change these values ( $P = .23-.98$ ). Notably, there was no significant change in tWSS in the distal unstented renal artery after placement of a proximal stent ( $32.7 \pm 11.8$  dynes/cm<sup>2</sup> vs  $29.6 \pm 13$  dynes/cm<sup>2</sup>;  $P = .23$ ).

**Patient-specific 3D flow visualization.** Hemodynamic data was also visualized using surface and volume rendering. This allowed for 3D visualization of parameters

of interest. For example, region-specific changes in tWSS were able to be observed, with one patient demonstrating fewer areas of high tWSS (>70 dynes/cm<sup>2</sup>) (Fig 5, A and B) and one patient demonstrating increased areas of high tWSS (Fig 5, C and D) after fEVAR. In addition, a patient with a 24-mm main body endograft with significant renal graft fabric protruding into the aortic lumen demonstrated significantly disturbed local flow and velocity fields following fEVAR (Fig 6, A and B), which was associated with areas of lower velocity recirculation (Fig 6, C).

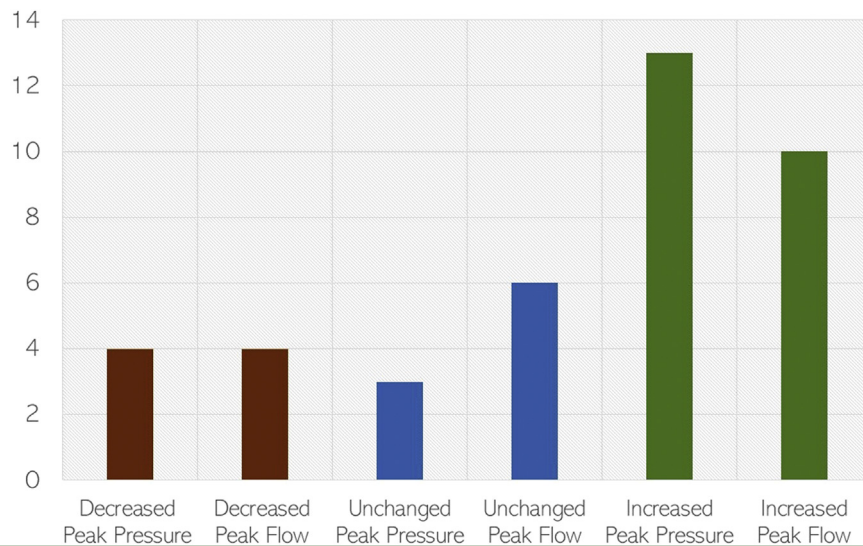
## DISCUSSION

The complexity of endovascular devices available for aneurysm repair have significantly increased over the last decade, with multibranch and fenestrated endografts gaining increased adoption as the standard of care for treating complex aortic aneurysms in patients at high physiologic risk. These devices use stent graft branches that significantly alter the normal arterial flow geometry to preserve visceral perfusion. In this study, we describe a pipeline for using advanced computational techniques to conduct detailed evaluations of the hemodynamic consequences of fEVAR and renal branch graft implantation. After an investigation of 10 patients, we found that fEVAR results in only subtle changes to the aortic and branch arterial pressure and

**Table II.** Simulated aortic and arterial branch peak and mean arterial pressures and flow rates

	Preoperative		<i>P</i> value	Postoperative		<i>P</i> value
	Peak pressure (mm Hg)	Peak pressure (mm Hg)		Mean pressure (mm Hg)	Mean pressure (mm Hg)	
Proximal aorta	136.9 ± 8.7	140.3 ± 11.1	.02	100.9 ± 7.2	101.7 ± 6.9	.04
Celiac artery	128.7 ± 12.2	125.8 ± 14.0	.65	98.2 ± 8.1	97.2 ± 8.5	.64
Superior mesenteric artery	128.4 ± 13.5	127.3 ± 14.6	.96	97.8 ± 8.4	97.3 ± 8.6	.57
Renal artery	128.9 ± 11.8	131.6 ± 14.8	.04	97.3 ± 8.1	98.3 ± 8.7	.30
Distal aorta	138.8 ± 8.5	141.7 ± 11.9	.17	100.9 ± 7.1	101.7 ± 6.9	.06
	Peak flow (mL/sec)	Peak flow (mL/sec)	<i>P</i> value	Mean flow (mL/sec)	Mean flow (mL/sec)	<i>P</i> value
Celiac artery	42.3 ± 9.0	40.1 ± 10.8	.72	8.9 ± 1.6	8.7 ± 1.5	.64
Superior mesenteric artery	47.4 ± 10.0	45.9 ± 12.6	.64	10.7 ± 1.8	10.6 ± 1.9	.28
Renal artery	16.9 ± 3.5	17.5 ± 3.8	.04	7.8 ± 1.2	7.8 ± 1.2	.92
Distal aorta	92.0 ± 20.3	95.5 ± 23.2	.16	17.9 ± 4.5	18.0 ± 4.6	.06

Values displayed as mean ± standard deviation. *P* values are based on paired analysis (signed rank-sum test).

**Fig 2.** Histogram of changes in renal artery hemodynamics between preoperative and postoperative flow simulations. The majority of stented renal arteries exhibited improved hemodynamic performance after fenestrated endovascular aneurysm repair (fEVAR).

flow rates, with no significant changes to calculated branch vessel wall shear stress after graft implantation.

In the current literature, CFD techniques have been applied to evaluate fEVAR in only a few limited studies.<sup>21,22,24</sup> Kandail et al<sup>21</sup> studied the effect of flared intra-aortic renal stent grafts in fEVAR using idealized hypothetical models. Using controlled experiments to study the theoretical effect of differences in flare angle and degree of graft protrusion, they found that changes in flare geometry had a negligible effect on the time dependence of renal flow waveforms. However, they also found significant local streamline flow disturbances owing to the altered geometry, suggesting that this may increase thrombogenicity at the renal ostia. We found a similar finding of low velocity flow adjacent to renal flares

in our study, particularly in patients with a high ratio of flared renal graft length to main body endograft diameter ratio. Further research to quantify this disturbance in a larger cohort of patients is an area of significant interest.

Using the same technique of creating idealized models, Kandail et al<sup>22</sup> also created controlled computational experiments comparing both antegrade and retrograde branch graft designs with fenestrated graft designs. They found that fenestrated branch grafts outperformed both antegrade and retrograde branches in terms of maximizing the renal flow rate.<sup>22</sup> By comparison, in our study we observed improved computationally estimated renal flow rates observed in 7 of 10 patients and only 1 patient in our study showing marginally decreased renal

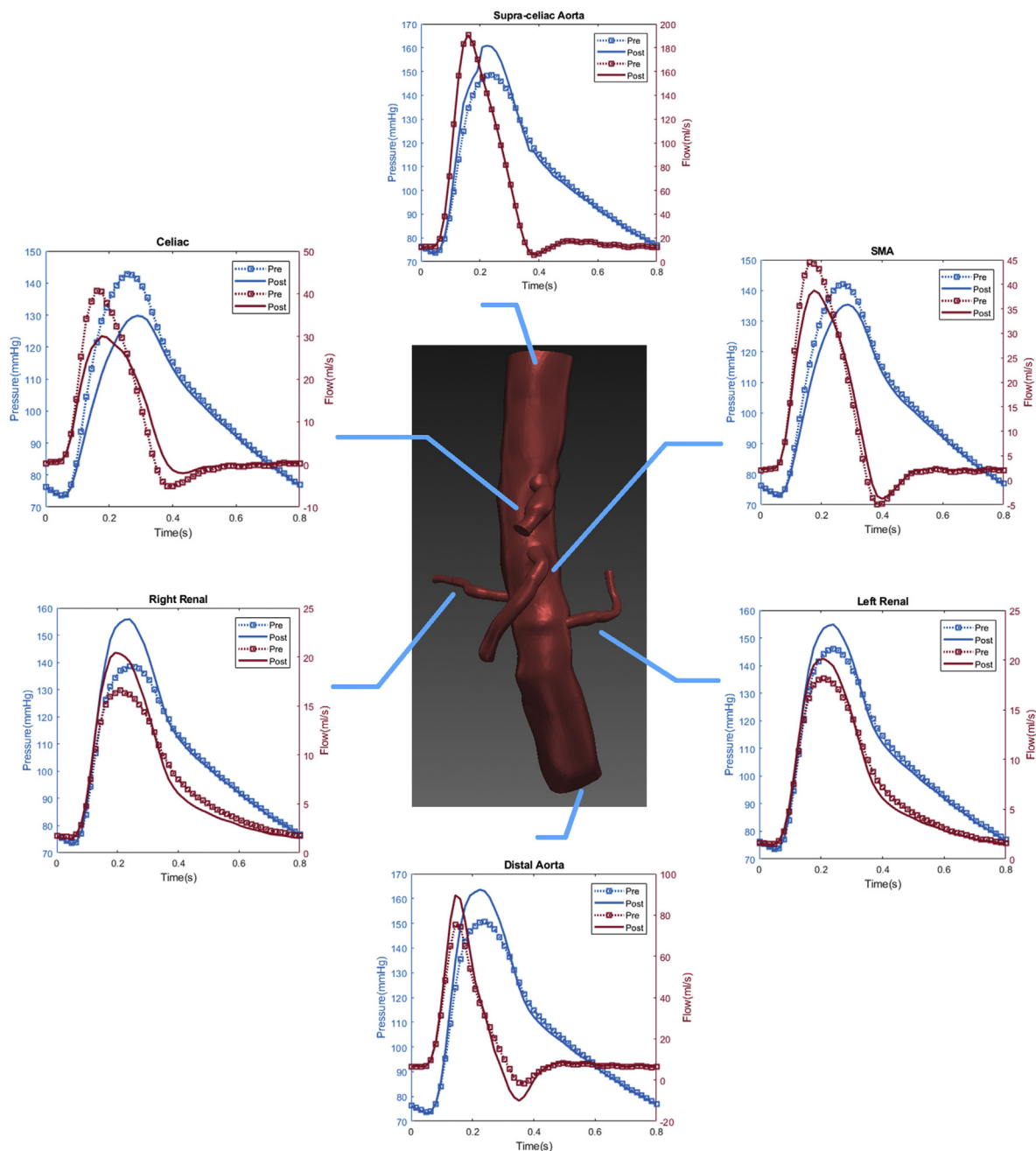


**Fig 3.** Representative flow simulation results of a patient treated with a 26-mm ZFEN graft. The calculated aortic and arterial branch pressure are displayed at the model inlets and outlets. Red lines depict flow waveforms and blue lines depict pressure waveforms. The dotted line depicts the preoperative results and the solid line depicts the postoperative results. In this patient, increased peak pressure and peak flow were observed in the bilateral renal arteries and proximal and distal aorta, whereas a decreased peak pressure and flow was observed in the superior mesenteric artery and celiac arteries after fenestrated endovascular aneurysm repair (FEVAR).

pressure and flow rates. These findings are in congruence with those reported by Kandail et al. Further investigations combining CFD analysis with invasive angiography or PC-MRI are necessary to clinically validate our findings.

In contrast, Suess et al<sup>24</sup> used CFD techniques to focus on an evaluation of the hemodynamic parameters

associated with near wall stresses, including tWSS and oscillatory shear index. They compared idealized models of fenestrated, antegrade branch, retrograde branch, and a novel manifold graft design with longer bridging stents deployed more proximally in the thoracic aorta. They found that longer bridging grafts deployed in a manifold

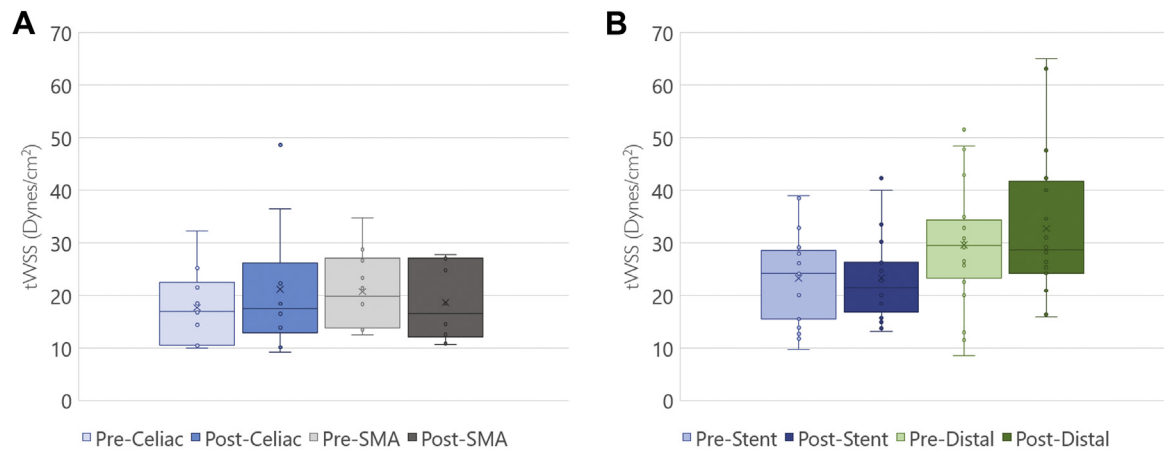


**Fig 4.** Calculated time-averaged wall shear stress (tWSS) of the vessel lumen of visceral (A) and renal (B) arterial branches. All measured tWSS values were within the homeostatic range of 10 to 70 dynes/cm<sup>2</sup>. There were no observed differences in the stented or unstented portions of the renal arteries after fenestrated endovascular aneurysm repair (fEVAR).

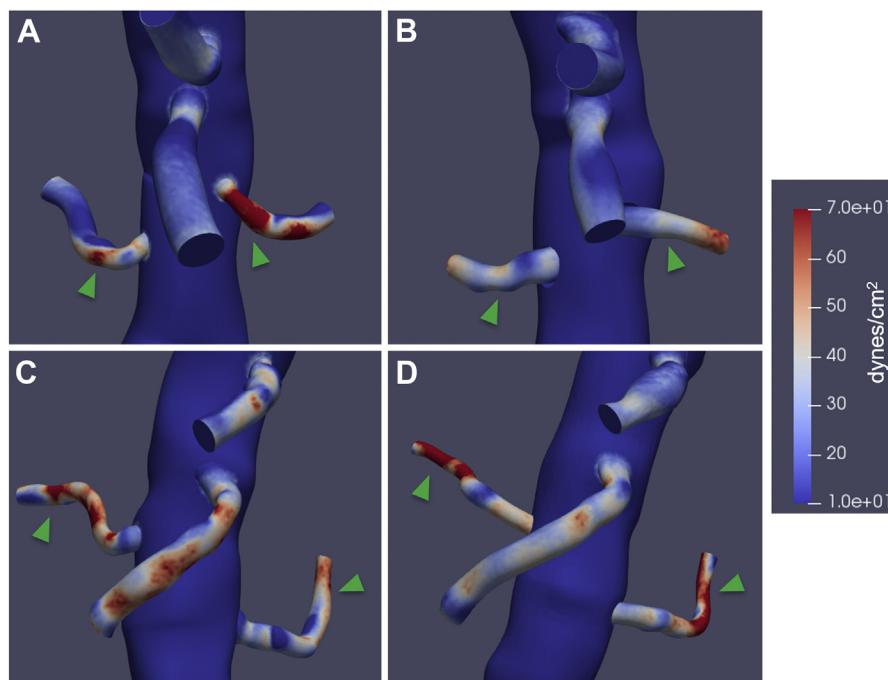


**Fig 5.** Graphically displayed representative images of time-averaged wall shear stress (tWSS) in a patient with decreased areas of renal artery tWSS between preoperative (A) and postoperative (B) models, compared with a patient with increased areas of tWSS in the renal arteries between preoperative (C) and postoperative (D) models.

design resulted in improved tWSS and near wall shear index profiles compared with fenestrated and traditional branch graft designs.<sup>24</sup> However, these findings were described more qualitatively. By comparison, we did not find any statistically significant changes to tWSS between preoperative and postoperative models in either proximal or distal renal arteries. All measured tWSS values in our study were within the homeostatic

range of 10 to 70 dynes/cm<sup>2</sup>. A tWSS of less than 10 dynes/cm<sup>2</sup> is prone to atherogenesis, whereas those of more than 70 dynes/cm<sup>2</sup> are prone to thrombosis.<sup>34</sup> A low tWSS has also been shown to correlate with areas of thrombus deposition and rupture in abdominal aortic aneurysms.<sup>35,36</sup> It is important to note that these studies, owing to using idealized models, in our opinion are limited in their clinical applicability of findings because

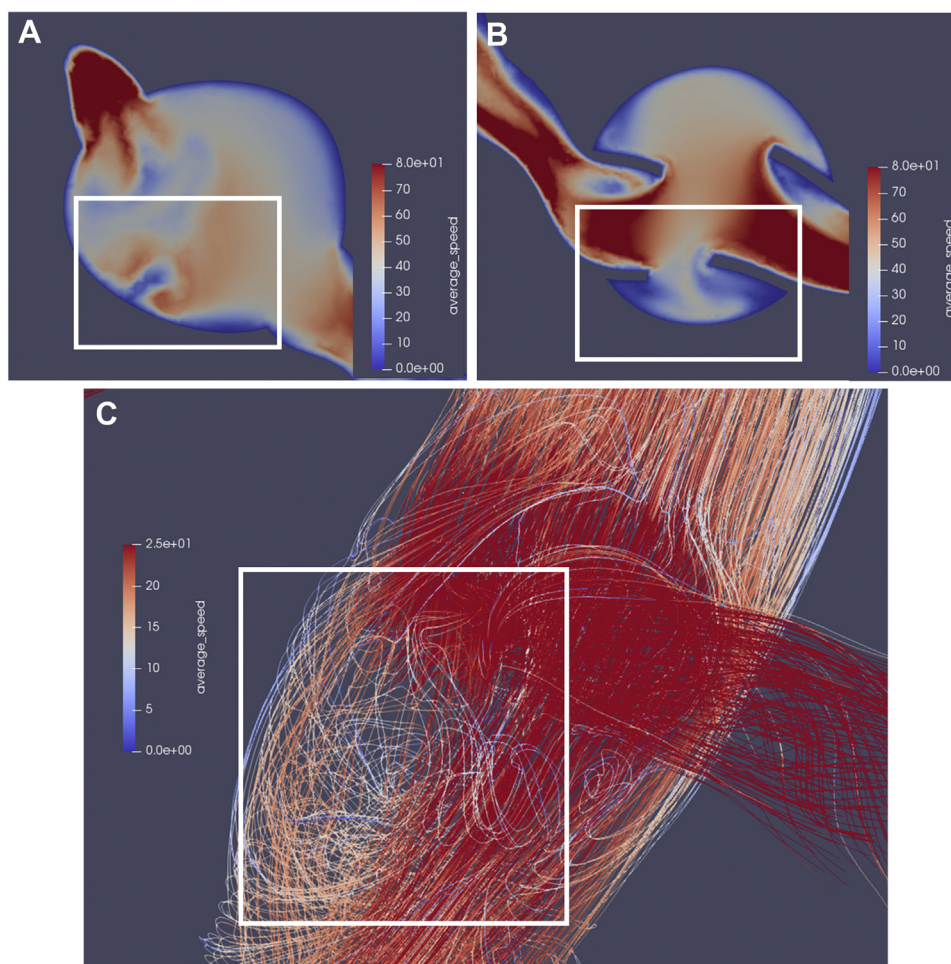


**Fig 6.** **A**, Preoperative two-dimensional (2D) axial velocity field demonstrating relatively minor flow disturbance along the anterior aortic wall. **B**, Postoperative axial velocity field demonstrating significant increased areas of low speed blood flow in the area between renal graft flare segments and **(C)** a sagittal view of a three-dimensional (3D) postoperative streamline simulation depicting areas of significant loss of speed and loss of laminar flow immediately adjacent to and inferior to the intra-aortic renal graft fabric protrusions. The white box depicts the same region of interest between panels.

changes in the hemodynamics between the preoperative and postoperative anatomy are unable to be compared using appropriate paired statistical analysis.

CFD techniques, however, have been used to analyze real-world outcomes after chimney EVAR. Tricarico et al<sup>20</sup> evaluated six patients who had undergone parallel chimney grafting, of which four patients had at least one occluded chimney graft. In this cohort, they found that hemodynamic signatures including a high systolic pressure gradient and systolic wall shear stress of more than 35 Pa (350 dynes/cm<sup>2</sup>) were predictive of graft occlusion.<sup>20</sup> Segalova et al<sup>23</sup> also explored the effect of bare metal strut coverage of renal arteries during infrarenal EVAR. In a study involving three patients treated with an endframe device (ie, Nellix), they found that the presence of endframe struts covering the renal ostia was minimal, with no significant detected disturbances in pressure, volumetric flow, or shear stress.<sup>23</sup>

It is important to discuss our results in the context of risk of long-term renal function decline after complex EVAR. Our group has previously reported on approximately a 20% to 30% risk of renal function decline after both chimney and fenestrated EVAR.<sup>8,37</sup> Interestingly, we found that all patients with computationally estimated increases in renal perfusion did not develop renal function decline during follow-up, whereas those with no change or decreased estimated renal perfusion suffered from renal function decline during follow-up. These data are limited by a small sample size and should be interpreted with caution. However, they highlight a highly interesting avenue of future investigation owing to the importance of optimizing long-term renal function in these patients. In addition, it should be noted that this study purposefully excluded patients who developed any thrombotic complications postoperatively (eg, renal stent thrombosis). As such, our results cannot determine

the potential clinical applicability of CFD analysis for predicting future thrombotic events, which is of critical importance for optimizing clinical outcomes. Future work involving a larger cohort of patients with and without complications is thus required to further explore this potential application.

We also noted a small, but statistically significant, increase in the peak aortic pressure measured at the aortic inlet after fEVAR. To our knowledge, this finding has not been reported or investigated after fEVAR or infrarenal EVAR. This measured change is likely reflective of the drastic decrease in aortic diameter after repair, thus increasing overall resistance within the 3D model; therefore, calculated pressures at the inlet are given equivalent in-flow conditions. However, this finding was not observed for all patients. More research is required to validate these findings clinically and determine any potential clinical implications.

Multiple limitations to this study exist and are worth discussion. PC-MRI data were not available preoperative or postoperatively for model validation and thus inflow and boundary conditions were created based on previously validated studies on patients with infrarenal abdominal aortic aneurysms. This process also required an estimation of flow fractions to each abdominal branch vessel based on average human values from the existing literature, and thus may be inaccurate for patients with significant celiac or mesenteric artery stenosis, in addition to any patient-to-patient variability. Large deviations from true physiologic values would affect not only perfusion metrics (eg, pressure and flow), but also affect measures local wall stresses and velocity fields. Future work may incorporate PC-MRI studies into the simulation pipeline to extract truly patient-specific inlet and outlet boundary conditions, and provide further validation of our methods.

For the purposes of model simplification and decreasing the computational cost, the lumbar and iliac arteries were excluded from analysis. This choice may result in differences of computationally derived flow patterns, particularly in patients with altered iliac anatomy (eg, iliac occlusive disease), where adjusted preoperative outlet boundary conditions would have to be created to account for the presence of higher distal resistance. Of note, no patients with preexisting iliac occlusive disease were included in this pilot study. Simulations were also performed using rigid walls. Although grafts behave as nearly rigid *in vivo*, native arterial flow is best modelling using deformable wall simulations. This goal can be accomplished by using coupled momentum methods for determining fluid-solid interaction, which require an order of magnitude increase in computational resources.<sup>38</sup> However, it has been shown that the differences between rigid wall and fluid-solid interaction deformable wall simulations have minimal impact on calculated hemodynamic parameters in the abdominal

aorta, with tWSS and oscillatory shear index values differing only by approximately 5% between methods.<sup>39</sup> Nonetheless, hemodynamic analysis is not able to calculate force vectors affecting the stent structure from either pulsatile or respiratory-induced motion. These external forces are key factors as they pertain to mechanical methods of graft failure, such as material fatigue and stent fracture, and are better investigated using other analytical or bench models.<sup>40,41</sup>

To our knowledge, this study is the first to analyze postoperative changes after fEVAR in a larger cohort of real-world patients. We described a CFD simulation pipeline with open source software that may be used by surgeon-scientists to explore in detail the hemodynamic performance of fEVAR. Specific strengths of our study include the use of both CT scans and allometrically scaled inflow conditions, which represents a unique combination patient-specific modelling that has to date not yet been applied to patients undergoing complex EVAR. The input data to create these models are routinely collected preoperative and postoperatively, as such our methods and pipeline can be used at many institutions. In the future, these methods may be applied to branched and mixed endograft designs, which are currently available for use in Europe and in clinical testing in the United States. Preoperative patient-specific computational surgical simulation may also be performed.<sup>25</sup> The computational time and costs associated with flow simulations will inevitably decrease as technology evolves. Thus, we believe that CFD simulation is an exciting emerging tool in the armamentarium of the modern vascular surgeon that may aid in preoperative and postoperative decision-making for the endovascular treatment of complex aortic aneurysmal disease.

## CONCLUSIONS

In a pilot study involving a selected cohort of patients who underwent uncomplicated fEVAR, patient-specific flow modelling was a feasible method for assessing the hemodynamic performance of various two-vessel fenestrated device configurations and revealed subtle differences in computationally derived peak branch pressure and blood flow rates. Structural changes in aortic flow geometry after fEVAR does not seem to affect computationally estimated renovisceral branch perfusion or wall shear stress adversely. Additional studies with invasive angiography or PC-MRI are required to clinically validate these findings.

## AUTHOR CONTRIBUTIONS

Conception and design: KT, AM, JL

Analysis and interpretation: KT, WY

Data collection: KT

Writing the article: KT

Critical revision of the article: KT, WY, AM, JL

Final approval of the article: KT, WY, AM, JL

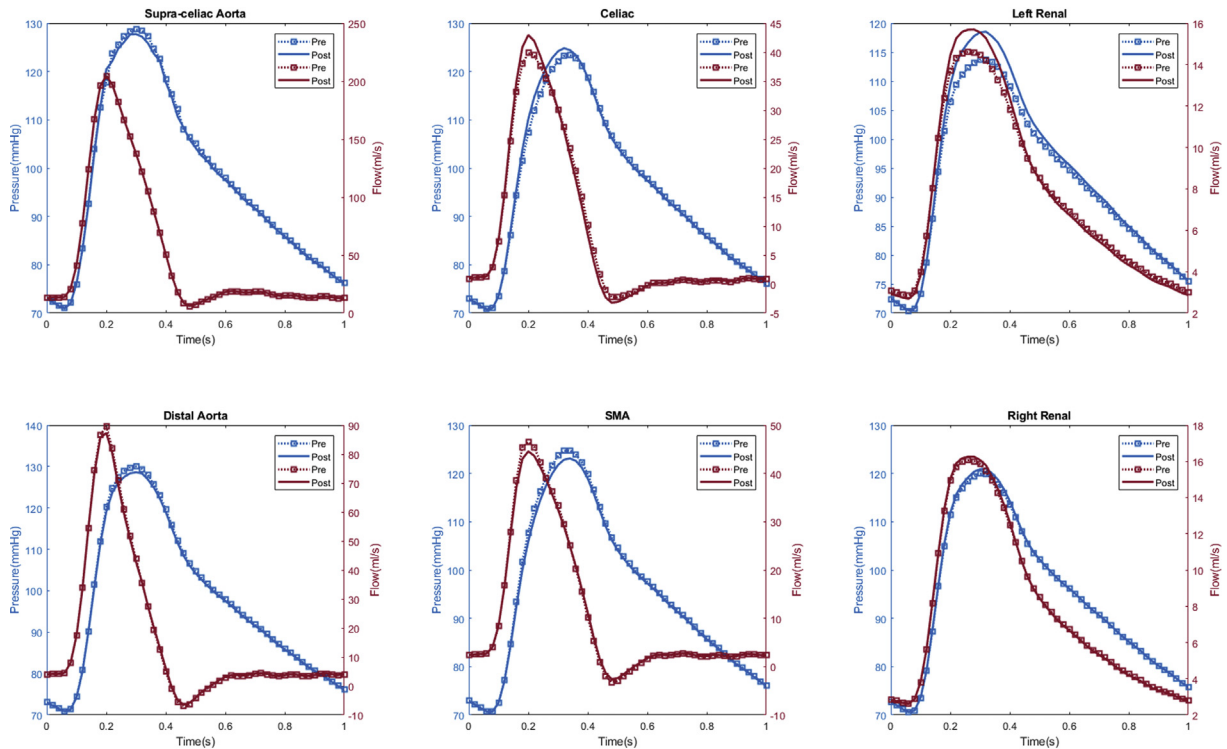
Statistical analysis: KT  
Obtained funding: am  
Overall responsibility: JL

## REFERENCES

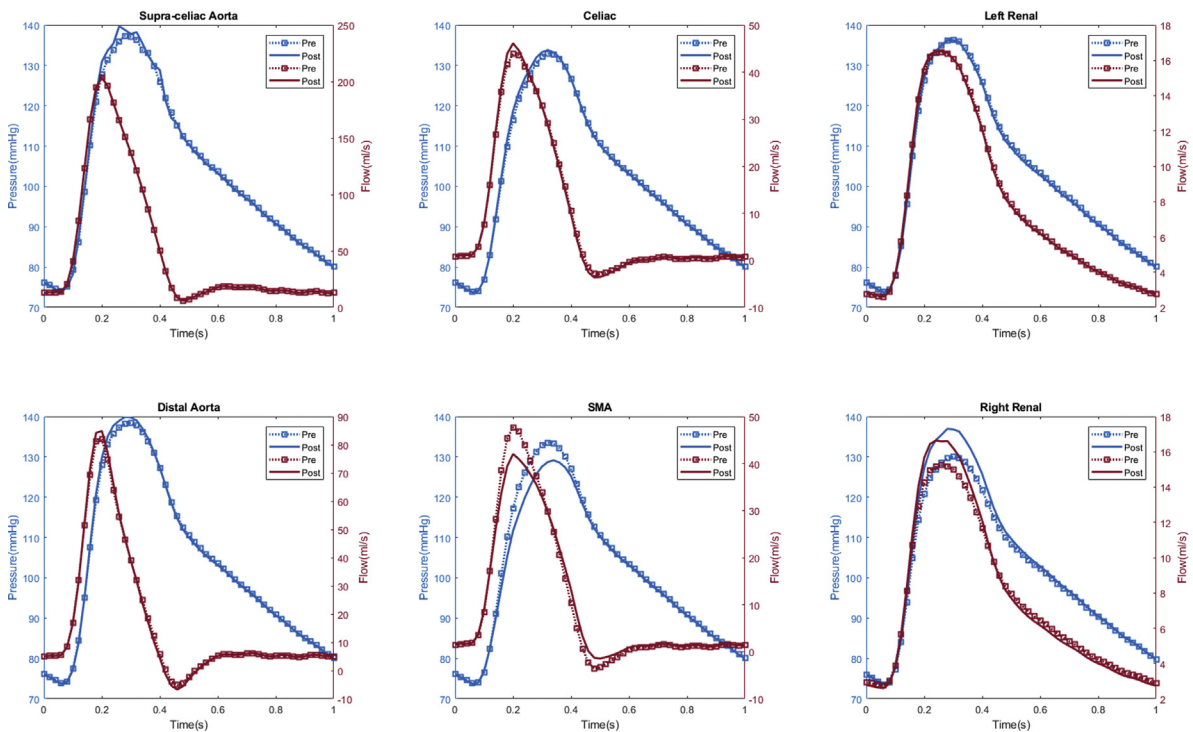
1. Suckow BD, Goodney PP, Columbo JA, Kang R, Stone DH, Sedrakyan A, et al. National trends in open surgical, endovascular, and branched-fenestrated endovascular aortic aneurysm repair in Medicare patients. *J Vasc Surg* 2018;67:1690-7.
2. Timaran DE, Knowles M, Ali T, Timaran CH. Fenestrated endovascular aneurysm repair among octogenarians at high and standard risk for open repair. *J Vasc Surg* 2017;66:354-9.
3. Study AMP. Results and factors affecting early outcome of fenestrated and/or branched stent grafts for aortic aneurysms. *Ann Surg* 2015;261:197-206.
4. Greenberg RK, Haulon S, Lyden SP, Srivastava SD, Turc A, Eagleton MJ, et al. Endovascular management of juxtarenal aneurysms with fenestrated endovascular grafting. *J Vasc Surg* 2004;39:279-87.
5. Glebova NO, Selvarajah S, Orion KC, Black JH, Malas MB, Perler BA, et al. Fenestrated endovascular repair of abdominal aortic aneurysms is associated with increased morbidity but comparable mortality with infrarenal endovascular aneurysm repair. *J Vasc Surg* 2015;61:604-10.
6. Canavati R, Millen A, Brennan J, Fisher RK, McWilliams RG, Naik JB, et al. Comparison of fenestrated endovascular and open repair of abdominal aortic aneurysms not suitable for standard endovascular repair. *J Vasc Surg* 2013;57:362-7.
7. de Souza LR, Oderich GS, Farber MA, Haulon S, Banga PV, Pereira AH, et al. Editor's choice – comparison of renal outcomes in patients treated by Zenith® fenestrated and Zenith® abdominal aortic aneurysm stent grafts in US prospective pivotal trials. *Eur J Vasc Endovasc Surg* 2017;53:648-55.
8. Tran K, Fajardo A, Ullery BW, Goltz C, Lee JT. Renal function changes after fenestrated endovascular aneurysm repair. *J Vasc Surg* 2016;64:273-80.
9. Tran K, McFarland G, Sgroi M, Lee JT. Duplex ultrasound surveillance of renal branch grafts after fenestrated endovascular aneurysm repair. *J Vasc Surg* 2019;70:1048-55.
10. Vignon-Clementel IE, Marsden AL, Feinstein JA. A primer on computational simulation in congenital heart disease for the clinician. *Prog Pediatr Cardiol* 2010;30:3-13.
11. Vignon-Clementel IE, Figueroa CA, Jansen KE, Taylor CA. Outflow boundary conditions for 3D simulations of non-periodic blood flow and pressure fields in deformable arteries. *Comput Methods Biomech Biomed Engin* 2010;13:625-40.
12. Taylor CA, Figueroa CA. Patient-specific modeling of cardiovascular mechanics. *Annu Rev Biomed Eng* 2009;11:109-34.
13. Kung E, Kahn AM, Burns JC, Marsden A. In vitro validation of patient-specific hemodynamic simulations in coronary aneurysms caused by Kawasaki disease. *Cardiovasc Eng Technol* 2014;5:189-201.
14. Zhu Y, Chen R, Juan YH, Li H, Wang J, Yu Z, et al. Clinical validation and assessment of aortic hemodynamics using computational fluid dynamics simulations from computed tomography angiography. *Biomed Eng Online* 2018;17:1-12.
15. Ku JP, Elkins CJ, Taylor CA. Comparison of CFD and MRI flow and velocities in an in vitro large artery bypass graft model. *Ann Biomed Eng* 2005;33:257-69.
16. Yang W, Chan FP, Reddy VM, Marsden AL, Feinstein JA. Flow simulations and validation for the first cohort of patients undergoing the Y-graft Fontan procedure. *J Thorac Cardiovasc Surg* 2015;149:247-55.
17. Zarins CK, Taylor CA, Min JK. Computed fractional flow reserve (FFTCT) derived from coronary CT angiography. *J Cardiovasc Transl Res* 2013;6:708-14.
18. Malinauskas RA, Hariharan P, Day SW, Herbertson LH, Buesen M, Steinseifer U, et al. FDA Benchmark Medical Device Flow Models for CFD Validation. *ASAIO J* 2017;63:150-60.
19. Steinman DA, Migliavacca F. Editorial: special issue on verification, validation, and uncertainty quantification of cardiovascular models: towards effective VVUQ for translating cardiovascular modelling to clinical utility. *Cardiovasc Eng Technol* 2018;9:539-43.
20. Tricarico R, He Y, Laquian L, Scali ST, Tran-Son-Tay R, Beck AW, et al. Hemodynamic and anatomic predictors of renovisceral stent-graft occlusion following chimney endovascular repair of juxtarenal aortic aneurysms. *J Endovasc Ther* 2017;24:880-8.
21. Kandail H, Hamady M, Xu XY. Effect of a flared renal stent on the performance of fenestrated stent-grafts at rest and exercise conditions. *J Endovasc Ther* 2016;23:809-20.
22. Kandail H, Hamady M, Xu XY. Comparison of blood flow in branched and fenestrated stent-grafts for endovascular repair of abdominal aortic aneurysms. *J Endovasc Ther* 2015;22:578-90.
23. Segalova PA, Venkateswara Rao KT, Zarins CK, Taylor CA. Computational modeling of shear-based hemolysis caused by renal obstruction. *J Biomech Eng* 2012;134:1-7.
24. Suess T, Anderson J, Danielson L, Pohlson K, Remund T, Blears E, et al. Examination of near-wall hemodynamic parameters in the renal bridging stent of various stent graft configurations for repairing visceral branched aortic aneurysms. *J Vasc Surg* 2016;64:788-96.
25. Van Bakel TM, Arthurs CJ, Van Herwaarden JA, Moll FL, Eagle KA, Patel HJ, et al. A computational analysis of different endograft designs for Zone 0 aortic arch repair. *Eur J Cardio-thoracic Surg* 2018;54:389-96.
26. Lan H, Updegrove A, Wilson NM, Maher GD, Shadden SC, Marsden AL. A re-engineered software interface and workflow for the open-source simvascular cardiovascular modeling package. *J Biomech Eng* 2018;140:0245011.
27. Updegrove A, Wilson NM, Mewkow J, Lan H, Marsden AL, Shadden SC. SimVascular: an open source pipeline for cardiovascular simulation. *Ann Biomed Eng* 2017;45:525-41.
28. Les AS, Yeung JJ, Schultz GM, Herfkens RJ, Dalman RL, Taylor CA. Supraceliac and infrarenal aortic flow in patients with abdominal aortic aneurysms: mean flows, waveforms, and allometric scaling relationships. *Cardiovasc Eng Technol* 2010;1:10-1007.
29. Si H. TetGen, a delaunay-based quality tetrahedral mesh generator. *ACM Trans Math Softw* 2015;41.
30. Williams LR, Leggett RW. Reference values for resting blood flow to organs of man. *Clin Phys Physiol Meas* 1989;10:187-217.
31. Taylor CA, Hughes TJR, Zarins CK. Finite element modeling of blood flow in arteries. *Comput Methods Appl Mech Eng* 1998;158:155-96.
32. Esmaily Moghadam M, Bazilevs Y, Hsia TY, Vignon-Clementel IE, Marsden AL. A comparison of outlet boundary treatments for prevention of backflow divergence with relevance to blood flow simulations. *Comput Mech* 2011;48:277-91.
33. Esmaily-Moghadam M, Bazilevs Y, Marsden AL. A new preconditioning technique for implicitly coupled multidomain simulations with applications to hemodynamics. *Comput Mech* 2013;52:1141-52.

34. Malek AM, Alper SL, Izumo S. Hemodynamic shear stress and its role in atherosclerosis. *JAMA* 1999;393:2035-42.
35. Boyd AJ, Kuhn DCS, Lozowy RJ, Kulbisky GP. Low wall shear stress predominates at sites of abdominal aortic aneurysm rupture. *J Vasc Surg* 2016;63:1613-9.
36. Zambrano BA, Gharahi H, Lim C, Jaber FA, Choi J, Lee W, et al. Association of intraluminal thrombus, hemodynamic forces, and abdominal aortic aneurysm expansion using longitudinal CT images. *Ann Biomed Eng* 2016;44:1502-14.
37. Lee JT, Varu VN, Tran K, Dalman RL. Renal function changes after snorkel/chimney repair of juxtarenal aneurysms. *J Vasc Surg* 2014;60:563-70.
38. Figueroa CA, Vignon-Clementel IE, Jansen KE, Hughes TJR, Taylor CA. A coupled momentum method for modeling blood flow in three-dimensional deformable arteries. *Comput Methods Appl Mech Eng* 2006;195:5685-706.
39. Looyenga EM, Gent SP. Examination of fluid-structure interaction in stent grafts and its hemodynamic implications. *Front Biomed Devices* 2018;2018:12-6.
40. Roos H, Tokarev M, Chernoray V, Ghaffari M, Falkenberg M, Jeppsson A, et al. Displacement forces in stent grafts: influence of diameter variation and curvature asymmetry. *Eur J Vasc Endovasc Surg* 2016;52:150-6.
41. Torsello GF, Herten M, Frank A, Müller M, Jung S, Torsello GB, et al. Performance of BeCraft and BeCraft+ stent-grafts as bridging devices for fenestrated endovascular aneurysm repair: an in vitro study. *J Endovasc Ther* 2019;26:787-94.

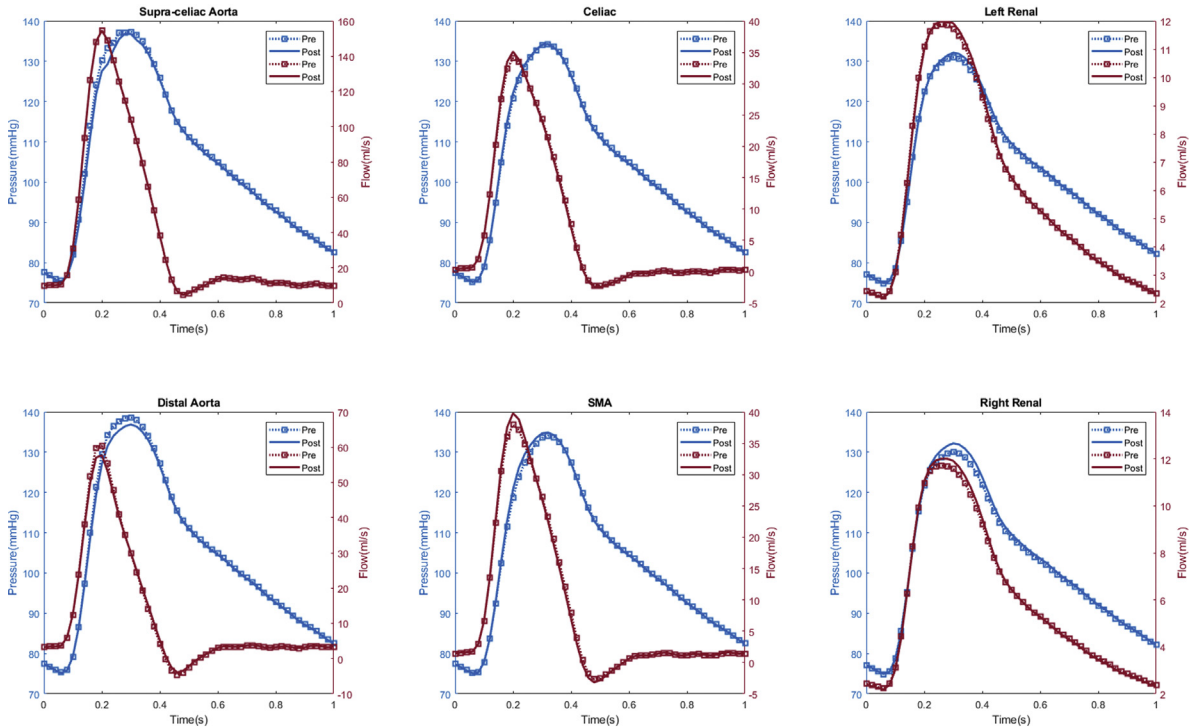
Submitted Apr 7, 2020; accepted Nov 30, 2020.



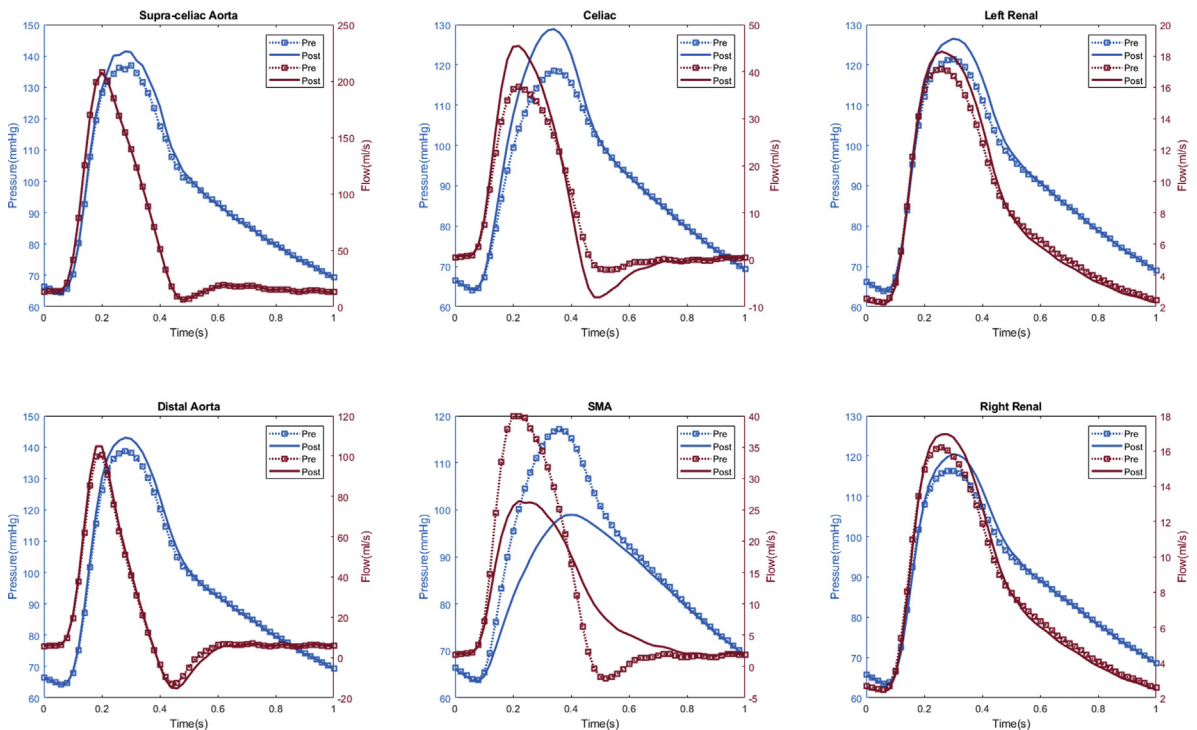
**Appendix 1.** Patient #1 calculated aortic and arterial branch pressure are displayed at the model inlets and outlets. The red lines depict flow waveforms and blue lines depict pressure waveforms. The dotted line depicts the preoperative results and the solid line depicts the postoperative results.



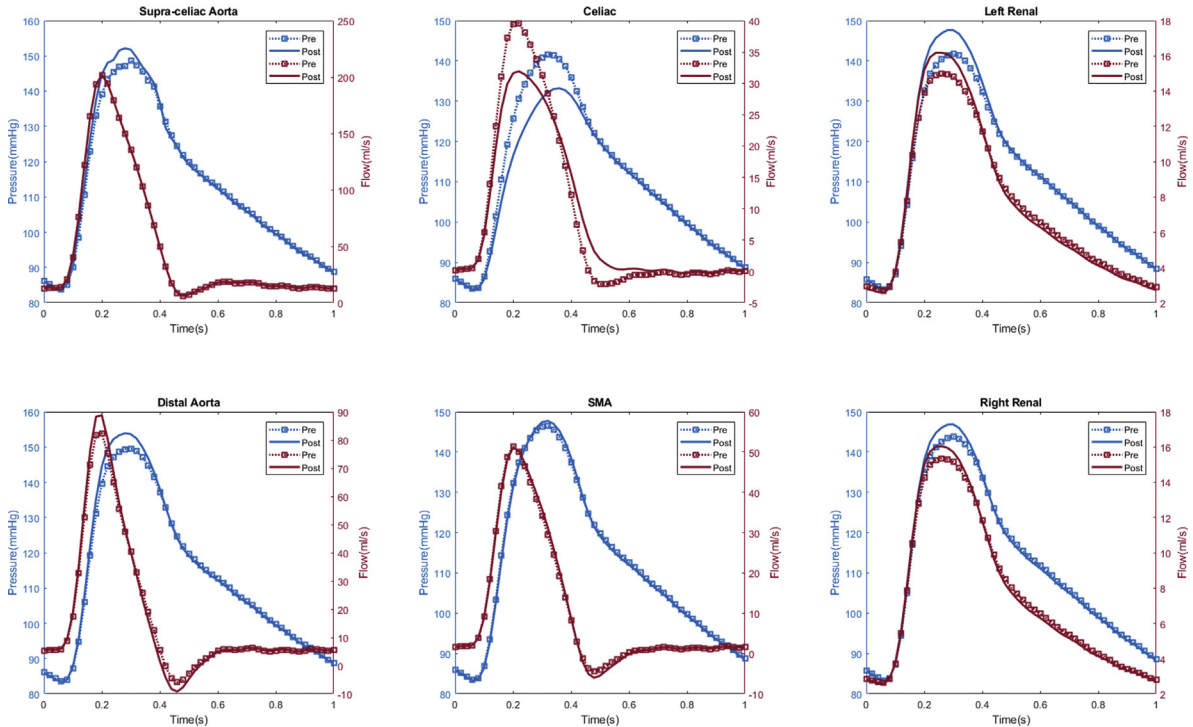
**Appendix 2.** Patient #2 calculated aortic and arterial branch pressure are displayed at the model inlets and outlets. The red lines depict flow waveforms and the blue lines depict pressure waveforms. The dotted line depicts preoperative results and the solid line depicts postoperative results.



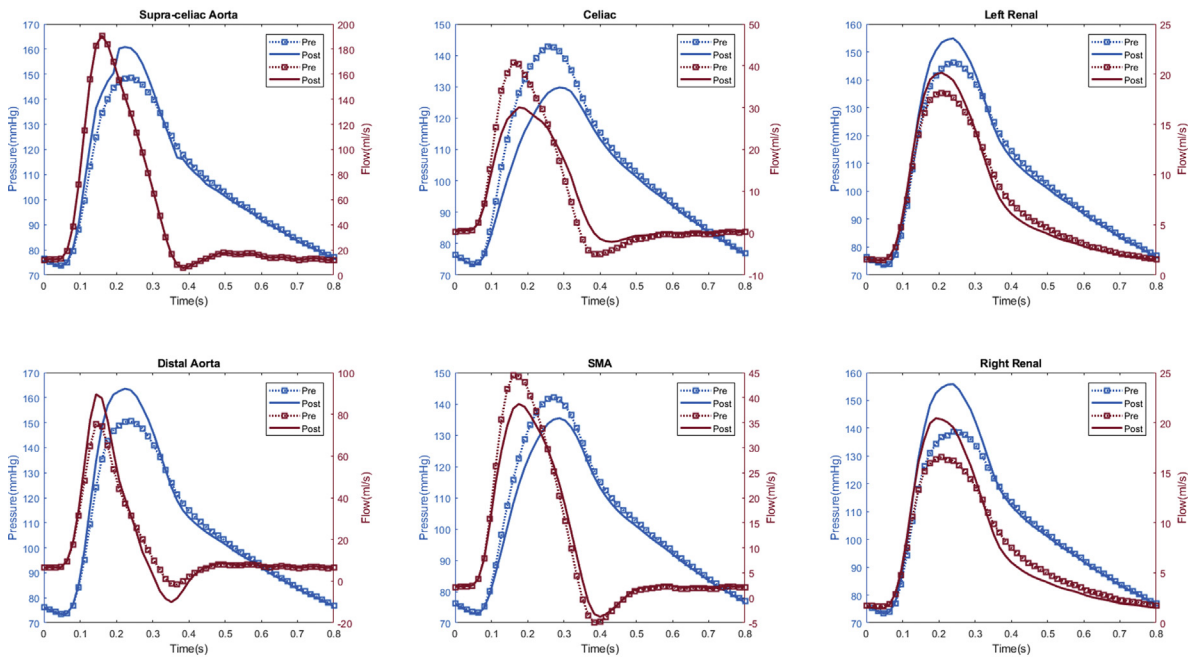
**Appendix 3.** Patient #3 calculated aortic and arterial branch pressure are displayed at the model inlets and outlets. The red lines depict flow waveforms and the blue lines depict pressure waveforms. The dotted line depicts preoperative results and the solid line depicts postoperative results.



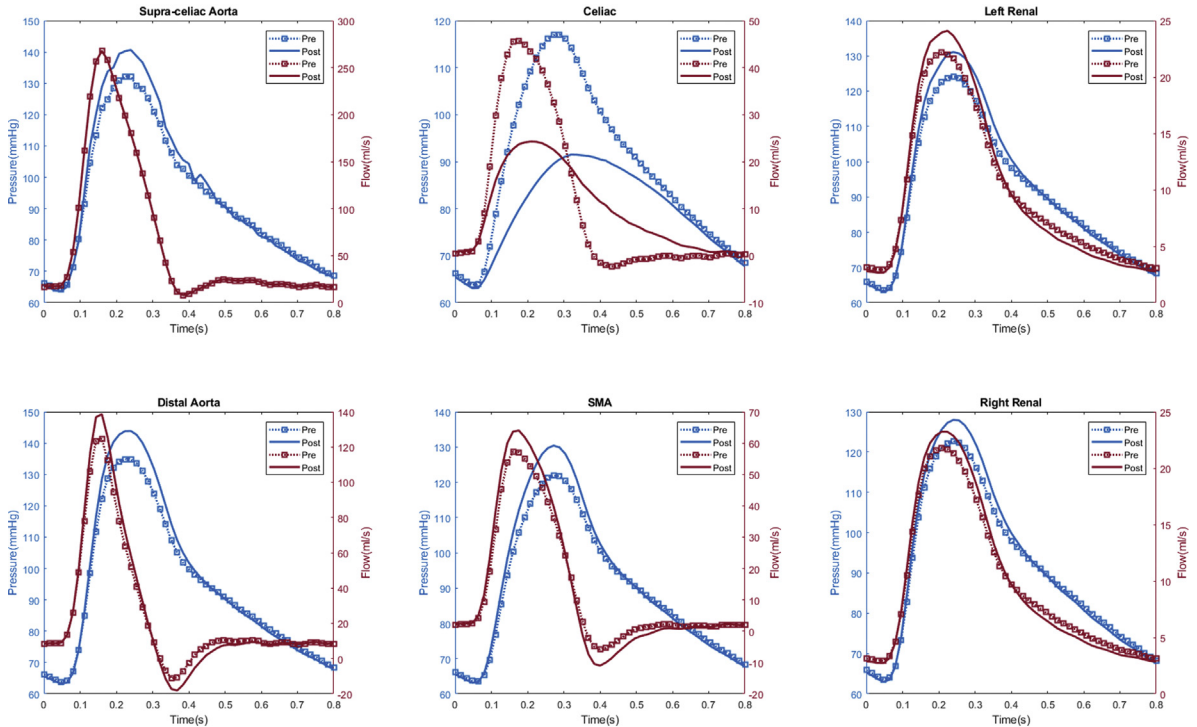
**Appendix 4.** Patient #4 calculated aortic and arterial branch pressure are displayed at the model inlets and outlets. The red lines depict flow waveforms and the blue lines depict pressure waveforms. The dotted line depicts preoperative results and the solid line depicts postoperative results.



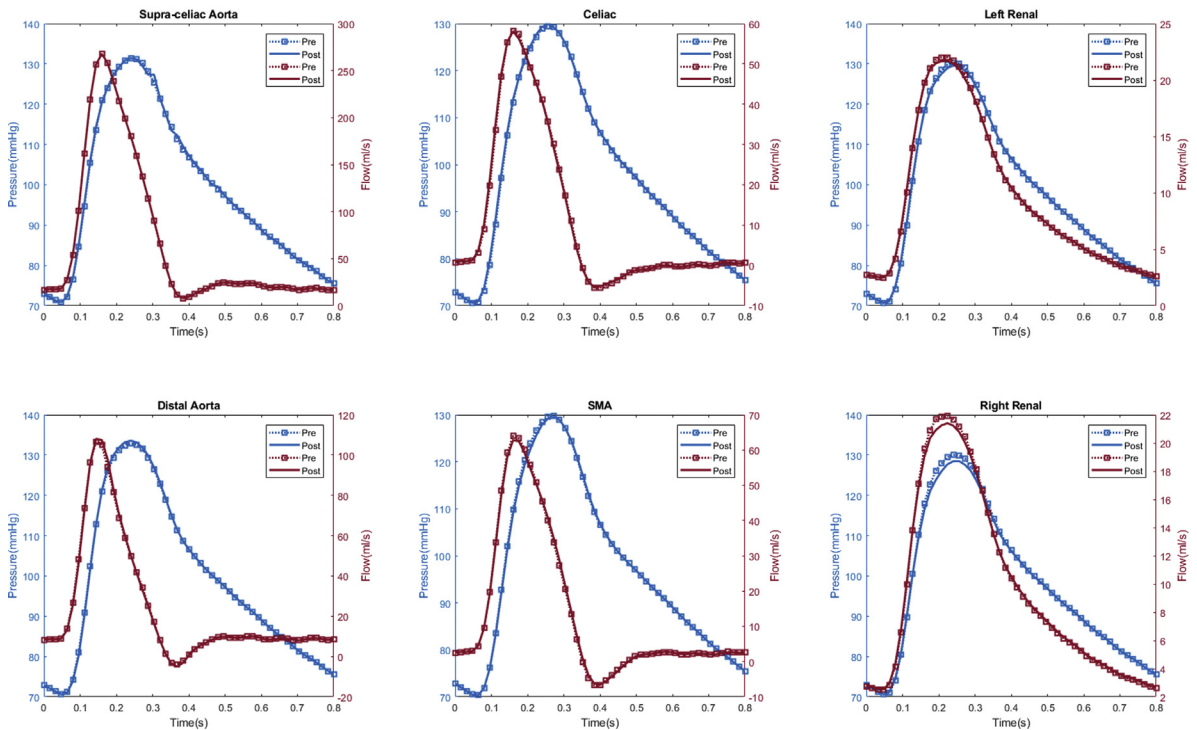
**Appendix 5.** Patient #8 calculated aortic and arterial branch pressure are displayed at the model inlets and outlets. The red lines depict flow waveforms and the blue lines depict pressure waveforms. The dotted line depicts preoperative results and the solid line depicts postoperative results.



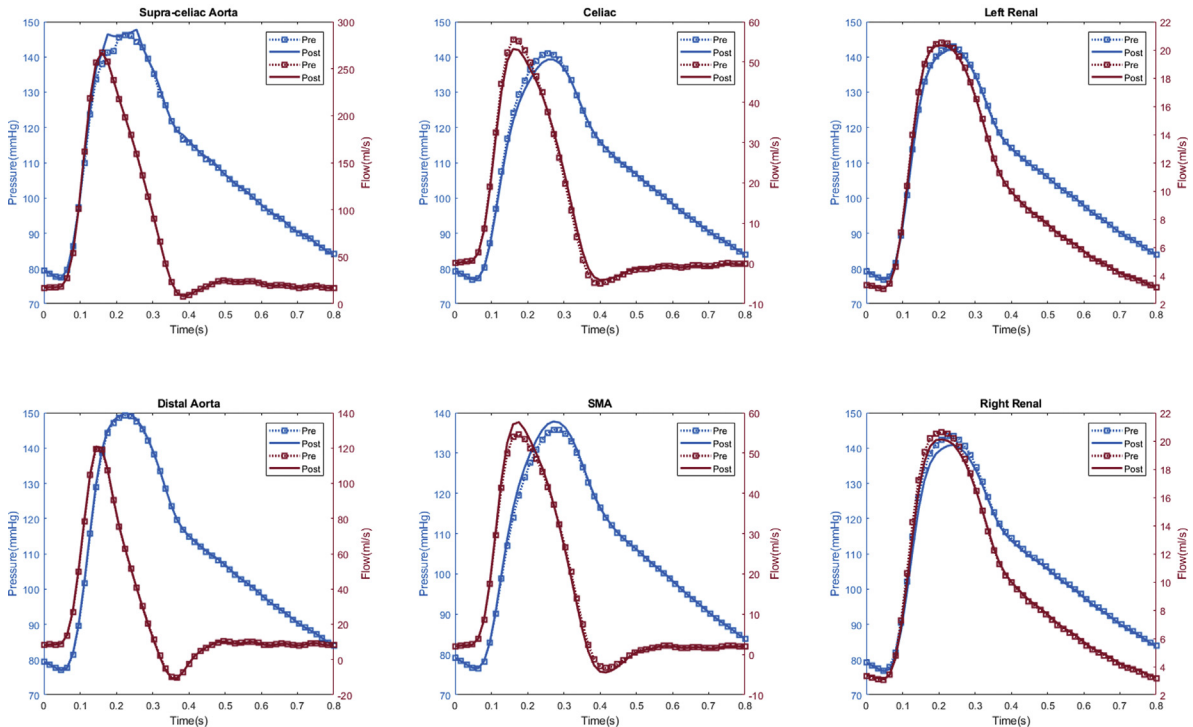
**Appendix 6.** Patient #9 calculated aortic and arterial branch pressure are displayed at the model inlets and outlets. The red lines depict flow waveforms and the blue lines depict pressure waveforms. The dotted line depicts preoperative results and the solid line depicts postoperative results.



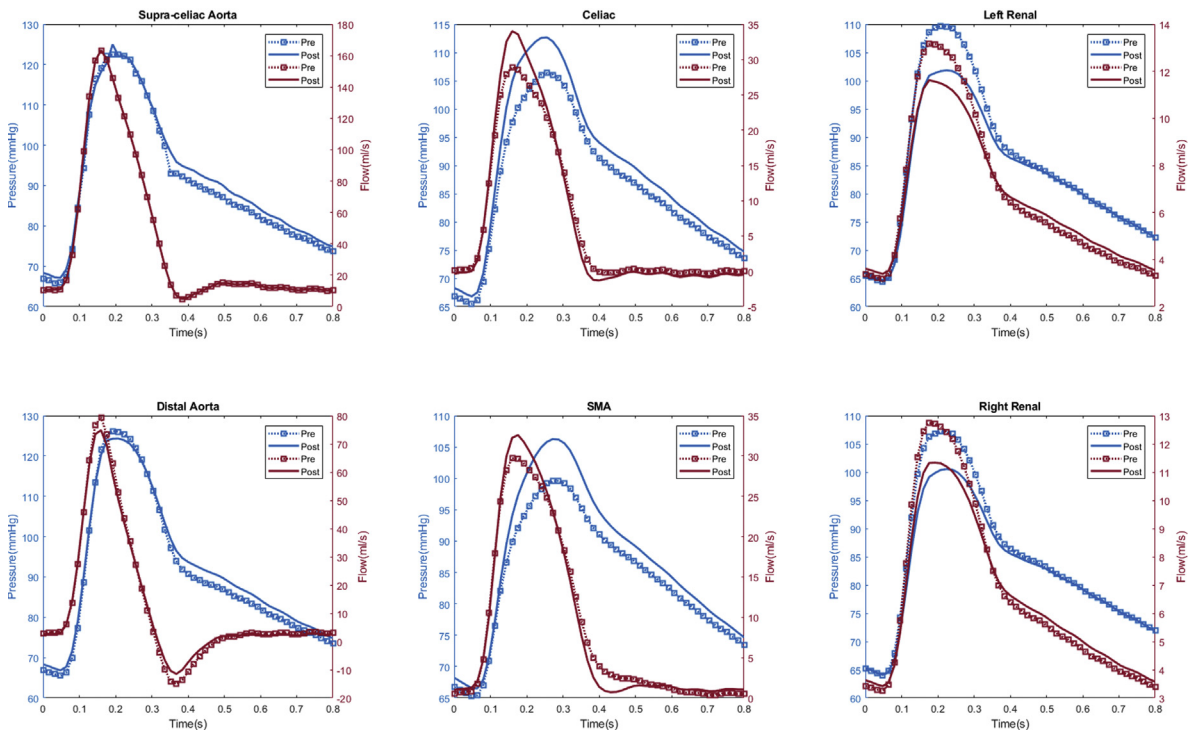
**Appendix 7.** Patient #10 calculated aortic and arterial branch pressure are displayed at the model inlets and outlets. The red lines depict flow waveforms and the blue lines depict pressure waveforms. The dotted line depicts preoperative results and the solid line depicts postoperative results.



**Appendix 8.** Patient #6 calculated aortic and arterial branch pressure are displayed at the model inlets and outlets. The red lines depict flow waveforms and the blue lines depict pressure waveforms. The dotted line depicts preoperative results and the solid line depicts postoperative results.



**Appendix 9.** Patient #7 calculated aortic and arterial branch pressure are displayed at the model inlets and outlets. The red lines depict flow waveforms and the blue lines depict pressure waveforms. The dotted line depicts preoperative results and the solid line depicts postoperative results.



**Appendix 10.** Patient #5 calculated aortic and arterial branch pressure are displayed at the model inlets and outlets. The red lines depict flow waveforms and the blue lines depict pressure waveforms. The dotted line depicts preoperative results and the solid line depicts postoperative results.